Earth and Space Science

RESEARCH ARTICLE
10.1029/2025EA004402

Global Hotspots for Sea-Level Changes: Decadal Extremes and Uncertainties From CMIP6 Models

Salah Basem Ajjur[1], **Emanuele Di Lorenzo**[1], **and Baylor Fox-Kemper**[1]

[1]Department of Earth, Environmental and Planetary Sciences, Brown University, Providence, RI, USA

Key Points:

- During 1950–2014, sea level rose in tide gauges (TGs) by 1.29 ± 0.32 mm/yr on average, varying between −10.0 and 6.52 mm/yr among regions
- The trend of sea level exceeded 2 times the global average in 26% of the regions analyzed (i.e., C. and E. North-America, N. Central-America, E. and C. Asia)
- Coupled Model Intercomparison Project Phase 6 simulations, especially earth system models, underestimate sea-level change over subtropical N. Atlantic regions and W. Central Asia, compared to TGs

Supporting Information:

Supporting Information may be found in the online version of this article.

Correspondence to:

S. B. Ajjur,
salah_ajjur@brown.edu

Citation:

Ajjur, S. B., Di Lorenzo, E., & Fox-Kemper, B. (2025). Global hotspots for sea-level changes: Decadal extremes and uncertainties from CMIP6 models. *Earth and Space Science*, *12*, e2025EA004402. https://doi.org/10.1029/2025EA004402

Received 7 APR 2025
Accepted 19 JUN 2025

Author Contributions:

Conceptualization: Salah Basem Ajjur, Emanuele Di Lorenzo, Baylor Fox-Kemper
Data curation: Salah Basem Ajjur
Formal analysis: Salah Basem Ajjur
Funding acquisition: Emanuele Di Lorenzo
Methodology: Salah Basem Ajjur, Emanuele Di Lorenzo, Baylor Fox-Kemper
Project administration: Emanuele Di Lorenzo
Supervision: Emanuele Di Lorenzo
Validation: Salah Basem Ajjur

Abstract Knowledge is limited regarding decadal extremes and uncertainties of sea-level change (SLC) at the regional scale, which necessitates the need for better understanding of these changes to enhance future coastal preparedness. To this end, we examined sea-level extremes for 23 World reference regions based on tide gauges (TGs) observations from 1950 to 2014. We then used these observations to evaluate the fidelity of climate models and earth system models (ESMs) participating in the Coupled Model Intercomparison Project Phase 6 (CMIP6), using trend analysis, correlation coefficient and Root Mean Square Error (RMSE) as metrics. Our findings show the spatial distribution of SLC varies between −10.0 and 6.52 mm/yr, with an area-weighted global average of 1.29 ± 0.32 mm/yr. Five regions display rapid increasing rates exceeding twice the global average: E. and C. North-America, N. Central-America, W. C. Asia, and S. E. Asia. Together, these regions constitute 26% of the total analyzed area. The CMIP6 simulations, especially ESMs, have a systematic underestimation of SLC, compared with TGs. We found poor agreement between CMIP6 simulations and TGs (weak correlation and larger RMSE) in subtropical North Atlantic regions and W. Central Asia. Our findings facilitate a multifactor hazard regional analysis that includes SLC alongside temperature, precipitation, and other parameters. It also identifies directions for future model development toward better detecting extremes and narrowing uncertainties in sea level simulations.

Plain Language Summary There is a dire need to incorporate sea-level science into immediate adaptation and defense plans. However, decadal extremes and uncertainties in sea level projections are unclear at regional scales. We investigated sea-level change (SLC) extremes from observations and assessed their uncertainties in the latest climate and earth system models, from 1950 to 2014, across the World regions. Results show significant extremes in North and Central America and Central Asia, with SLC rates exceeding twice the global average. Our findings highlight the need to improve models' simulations for accurate detection of SLC extremes and uncertainties.

1. Introduction

Sea-level change (SLC) poses an escalating threat to coastal regions worldwide, with far-reaching catastrophic consequences for human populations, coastal ecosystems, and the environment (Fox-Kemper et al., 2021). However, the scientific community has a deep uncertainty on the magnitude and timing of SLC projections. For example, our understanding of the contribution of land-based ice, such as the Greenland and Antarctic ice sheets and glaciers to SLC is limited (Fox-Kemper et al., 2021). Furthermore, internal climate variability and future forcings due to socioeconomic activities and greenhouse gas emissions are an important source of uncertainty (Kopp et al., 2023; Palmer et al., 2020). The latest assessment of SLC by the Intergovernmental Panel on Climate Change (IPCC) Sixth Assessment Report (AR6) reported a wide range of global mean sea level (GMSL) changes that varied, relative to 1995–2014, between 0.38 m (likely between 0.28 and 0.55 m) and 0.77 m (likely between 0.63 and 1.01 m) by the end-21st century, depending on the Shared Socioeconomic Pathways (Fox-Kemper et al., 2021). The AR6 also presented, for the first-time, additional projections for low-probability, high-impact scenarios, which included low confidence processes of accelerated ice sheet mass losses. The AR6, thus, provided an additional larger range of potential and associated uncertainty in SLC projections. Such uncertainty in SLC projections brings serious challenges for decision frameworks and coastal adaptation policies.

Previous research efforts partly explored the uncertainty of sea-level simulations in the previous phase of the Coupled Model Intercomparison Project. Slangen et al. (2017) compared GMSL changes in 12 CMIP5 models with tide gauge (TG) reconstructions during 1900–2007 and satellite altimetry estimates during 1993–2015. They used Representative Concentration Pathway (RCP8.5) projections to extend the CMIP5 analysis through the

Writing – original draft: Salah Basem Ajjur
Writing – review & editing: Salah Basem Ajjur, Emanuele Di Lorenzo, Baylor Fox-Kemper

period 2005–2015. Slangen et al. (2017) explained 75% of the GMSL changes before 2007. In a companion paper, Meyssignac et al. (2017) found a mean systematic underestimate of sea levels simulated by CMIP5, compared with observations at 27 TGs stations distributed worldwide. The underestimate was around 0.27 mm/yr. Palmer et al. (2020) compared mean sea level (MSL) projections in 21 CMIP5 models with 16 TG locations around the world. They found some TGs have large departures from the global mean which emphasized the importance of studying local variability of SLC. Deepa et al. (2021) assessed variability of CMIP5 sea level simulations, through 2100, over the Indo-Pacific Ocean. They found some variations in the amplitude and inter-model disagreement. For the period 2007–2018, Wang et al. (2021) reported an approximate identical trend, within the 90% confidence level, between sea level projections in the IPCC fifth Assessment Report (AR5), the IPCC's Special Report on the Ocean and Cryosphere in a Changing Climate, and TGs and satellite observations. The previously mentioned efforts focused on the CMIP5 models.

Using the latest Coupled Model Intercomparison Project Phase 6 (CMIP6) models, Lyu et al. (2020) assessed ocean dynamic sea level (DSL) simulations in CMIP6 models against observations. They showed a positive bias in DSL projections over the North Atlantic and Arctic. Similarly, C. Jin et al. (2023) evaluated the performance of CMIP6 simulations of global DSL, compared to CMIP5 simulations. They concluded some CMIP6 models perform better in detecting climatological norms as well as seasonal and interannual variability, but not decadal variability. Chen et al. (2023) assessed the performance of CMIP6 simulations of the climatological mean and interannual variance of DSL over the 40°S–40°N region. They found a large bias and model discrepancy in the North Atlantic subtropical region. Ferrero et al. (2021) evaluated the changes in DSL projections in CMIP6 models through 2100 using outputs from a 50-member CanESM5 ensemble as well as an ensemble of 27 other models. They highlighted the changes between DSL projections under different emission scenarios. C. Jin et al. (2024) categorized uncertainty sources in DSL projections from CMIP6 and an FGOALS-g3 large-ensemble experiment into internal variability, intermodel, and scenario-based uncertainty. They found a dominant contribution by intermodel uncertainty at basin and regional scales, in general. Other efforts aimed to analyze the risk associated with extreme sea levels with concurrent heatwaves (Zhou & Wang, 2024), storm surge and wave activity (Jevrejeva et al., 2023). Some literature studied SLC over specific regions, such as the North Sea (Jesse et al., 2024), Southeast Asia (Y. Jin et al., 2023), the Indian Ocean (Sajidh & Chatterjee, 2023; Sreeraj et al., 2022), and the UK shelf seas (Bulgin et al., 2023). For instance, Jesse et al. (2024) aimed to understand the processes that affect DSL changes in CMIP5 and CMIP6 simulations over the North Sea region. They found the Atlantic meridional overturning circulation to be an important predictor of regional dynamic SLC in CMIP6 models. Sajidh and Chatterjee (2023) assessed the performance of CMIP6 models over the Indian Ocean and found that CMIP6 models simulate the historical mean state of DSL reasonably well, but model skill varies across the latitude band of the Indian Ocean. Using high-resolution ocean simulations from MPI-ESM-ER (at approximately 0.1° grid resolution), C. Jin et al. (2023) and Y. Jin et al. (2023) aimed to understand the trend and variability of sea levels over Southeast Asia. They found the region to be extremely influenced by the El-Nino Southern Oscillation variability.

While much work has been done to assess CMIP6 simulations at various regional scales around the world, there is still much uncertainty left to address. There are several drivers of local differences in SLC, such as local meteorology, ocean volume (due to temperature variations), active local tectonic movement and anthropogenic activities for example, groundwater and gas extraction (Fox-Kemper et al., 2021). If CMIP6 models cannot replicate historical local observation, which is expected as they are meant to represent climate-scale and may not capture temporal and spatial variations of SLC at regional scales, then raising concerns regarding the skill of these models to project future SLC over uncertain regions is imperative. Such knowledge helps us identify directions for future model development toward improved detection of extremes and narrowing of uncertainties in sea level simulations.

In this study, we aim to (a) identify decadal extremes of SLC as observed by TGs and (b) evaluate the fidelity of SLC simulations in the latest CMIP6 experiment during 1950–2014. Since the configuration of climate models (CMs) is different than (earth system models [ESMs]) with regard to the modeled physics (see Séférian et al. (2019) for a comparison between CNRM-CM6-1 and CNRM-ESM2-1), we differentiate between both configurations while assessing CMIP6 data. A multi-model ensemble mean was created from 12 CMs (CMs MEM) and a multi-model ensemble mean was created from 14 ESMs (ESMs MEM). This study contributes to the existing literature in two ways. First, the regional analysis conducted in this study includes 23 World reference regions, as defined by the IPCC AR6 and documented by Iturbide et al. (2020). This can facilitate a multifactor

10.1029/2025EA004402

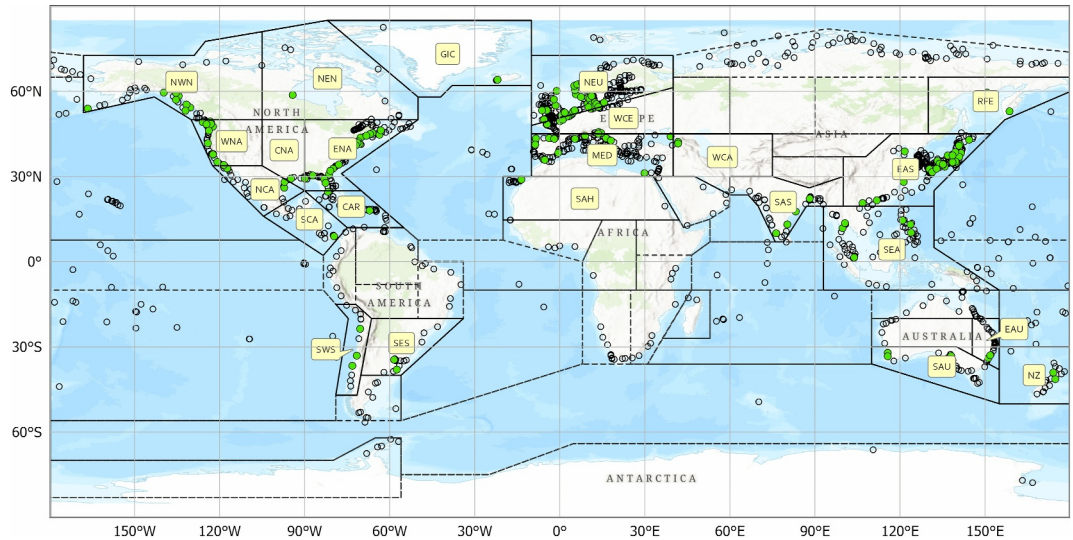

Figure 1. The locations of the Permanent Service for Mean Sea Level tide gauge (TG) stations within the Intergovernmental Panel on Climate Change AR6 reference regions (Iturbide et al., 2020). Hollow circles mark the locations of all TG stations while the 183 filtered TGs remaining after quality check, are marked by green circles and their regions are labeled with acronyms.

hazard analysis by including sea level alongside temperature and precipitation. Second, this study primarily focuses on a 20-year time interval window and thus makes the trends more sensible from a regional perspective through filtering out global modes of climate variability that would differ between the climate models and the observations (Lee et al., 2021).

2. Data

We use three sources of data: TG observations, satellite estimates, and CMIP6 simulations. Specific details about these sources are given below.

2.1. TGs Observations

We used monthly worldwide TGs data that is sourced from the Permanent Service for Mean Sea Level (PSMSL) (Holgate et al., 2013). Stations that are located in the polar regions were excluded and only those between 65°S and 65°N had undergone a three-step quality control to ensure data reliability. First, TGs that are missing over 20 years of data (30% of the study period) were rejected. Second, TGs with consequent missing records spanning more than 10 years were excluded from the analysis. Third, TG records that exhibit a sudden sea-level jump exceeding 50 cm between two consecutive months were disregarded. Following these quality control procedures, a total of 183 TG stations remained available for subsequent analysis, with their geographic locations illustrated in Figure 1. Information on the latitude, longitude, names, and locations of these TGs are summarized in Table S1 in Supporting Information S1. Of the filtered TG stations, some stations still had a gap in their observations. These gaps were not filled.

The PSMSL records are originally reduced to a revised local reference datum (~7 m below MSL) to avoid negative numbers in the resulting mean values (Holgate et al., 2013). Therefore, records were corrected and prepared for later comparison of relative SLC with CMIP6 models (see Section 2.3).

2.2. Satellite Estimates

We used satellite altimetry to compare SLC after 1993. Unlike TGs, satellite measures geocentric sea level only and hence are not influenced by Vertical Land Motion (VLM). Therefore, local VLM is typically inferred as the difference between TGs and satellite estimates (Gregory et al., 2019; Wöppelmann & Marcos, 2016). It is calculated as per Equation 1

$$\Delta R(r) = \Delta\eta(r) - \Delta F(r) \quad (1)$$

Where $\Delta R(r)$ represents the relative SLC, $\Delta\eta(r)$ is the geocentric SLC, and $\Delta F(r)$ is the VLM. We obtained VLM rates as a function of time determined by the Nevada Geodetic Laboratory (NGL). The NGL utilized existing networks of Global Navigation Satellite Systems (GNSS), TGs, and altimetry data to provide robust interpolated VLM approximates at PSMSL TGs locations. The analysis methods and estimate strategy are documented in Hammond et al. (2016, 2021). For altimetry data, the gridded monthly anomalies of sea level, with respect to the 1993–2012 mean, were acquired from the European Centre for Medium-Range Weather Forecasts (ECMWF) Copernicus Marine Service (CMEMS, 2018). The CMEMS data are based on observations from multiple altimeter missions from GEOSAT to Jason-3. Data are provided on a $0.25° \times 0.25°$ spatial grids, covering the period between January 1993 and August 2022 (acquired until December 2014, in this study, to enable comparison with CMIP6 simulations). The inverse barometer (IB) effect is initially removed from CMEMS altimetry data; however, data have not been corrected for Earth Gravity, Earth Rotation, and viscoelastic solid-Earth Deformation (GRD) effect (CMEMS, 2018). Therefore, we removed the GRD effect by subtracting the NGL estimates from the satellite altimetry. Next, the long-term seasonal signal (annual and semi-annual) was removed, and a 5-month running-mean filter was applied to avoid noise in monthly data. The time series altimetry estimates were extracted from the nearest available gridpoint to the coordinates of the filtered TGs.

2.3. CMIP6 Simulations

Monthly sea-level simulations, during 1950–2014 were obtained from 12 CMs to 14 ESMs participating in the CMIP6 (Table S2 in Supporting Information S1). We selected the first realization (r1i1p1f1) from each model. In CMIP6, the ocean dynamic SLC ($\Delta\xi$) is named "zos" and is defined as sea surface height above geoid, while the global-mean thermosteric SLC (h_θ) is named "zostoga" and is defined as the part of global mean SLC due to thermal expansion (Gregory et al., 2019). By definition, the DSL should always have zero global mean in CMIP6 models. Therefore, for each model, we first removed the global mean from original values, if found to be non-zero. The drifts in CMIP6 models were then removed from "zos" and "zostoga" variables using piControl simulations of corresponding runs. Since historical simulations are branched from a specific time in pre-industrial control runs, we identified this time and found the pre-industrial period that runs parallel to the historical simulations. Then, the long-term linear trend of piControl data was removed from historical simulations. Then, the long-term mean seasonal cycle was removed, and a 5-month running-mean filter was applied (Wang et al., 2021). Previous calculations were made for each CMIP6 model. All models were then bilinearly interpolated to a common grid resolution of $0.5° \times 0.5°$ and used to compute the CMs MEM and ESMs MEM. We calculated the sterodynamic SLC (ΔZ) as the sum of the ocean dynamic SLC and global-mean thermosteric SLC (h_θ).

$$\Delta Z(r) = \Delta\xi(r) + h_\theta \quad (2)$$

Next, the simulations from each CMIP6 model, as well as from each of the CMIP6 MEMs, were extracted at filtered TGs locations using the nearest gridpoint to the coordinates of the TGs. We recognize that h_θ calculations in CMs are different from ESMs Séférian et al. (2019). Figure 2 compares global-mean thermosteric SLC (h_θ) as estimated by CMs and ESMs. Note that one CM (GISS-E2-1-H) has significant different estimates for h_θ changes, relative to other CMs.

TGs measure relative SLC, so to compare relative SLC with CMIP6 simulations, the barystatic sea level effect, the GRD effect, and the inverted barometer effect should be removed, as per Equation 3 (Gregory et al., 2019)

$$\mathrm{SLC}(r) = \Delta Z(r) + h_b + \Delta\Gamma(r) - \mathrm{IB}(r) \quad (3)$$

Where $\Delta R(r)$ represents the sterodynamic SLC, h_b is the barystatic SLC (see below), $\Delta\Gamma$ is the GRD effect, and IB is the inverted barometer correction.

The barystatic SLC, also known as mass-driven SLC, is the part of GMSL rise which is due to the addition to (or the removal from) the ocean water mass that formerly resided within the land area or in the atmosphere. It is computed as per Equation 4

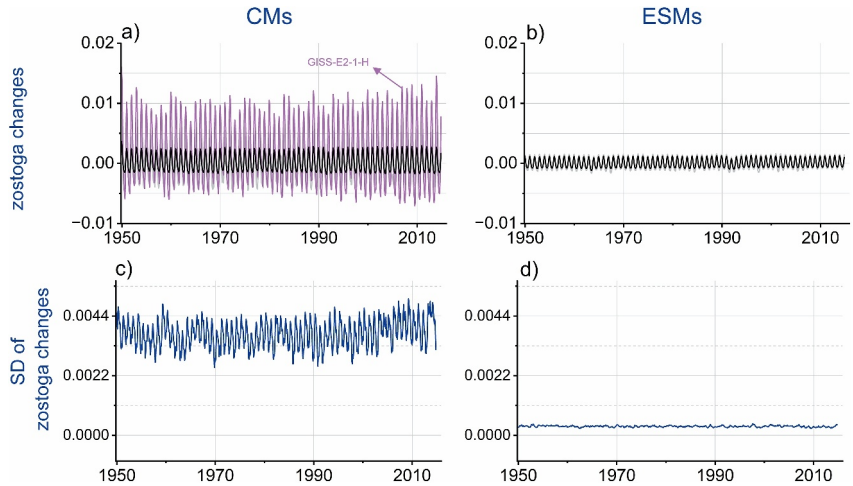

Figure 2. Comparison between global-mean thermosteric sea-level change (h_θ) as estimated by (a) climate models (CMs) and (b) earth system models (ESMs). The standard deviation of h_θ changes among CMs and ESMs is shown in panels (c, d).

$$h_b = \frac{\Delta M}{\rho_f A} \tag{4}$$

Where ΔM is the change in mass of the global ocean (from all contributors), ρ_f is freshwater density, while A is the ocean surface area (Gregory et al., 2019). The ΔM is calculated as the sum of SLC resulted from mass variations from land-ice (e.g., ice sheets, glaciers, etc.) and land water storage "LWS" (also called terrestrial water storage "TWS"), which represents the water stored as groundwater, soil moisture, reservoirs, lakes and rivers, seasonal snow and permafrost. Note that according to Gregory et al. (2019), the GRD label is a concept that unifies Glacial isostatic adjustment (GIA), and the contemporary GRD. It represents continuing changes in the solid Earth caused by past changes in land ice.

In this study, we got the barystatic SLC and GRD effect from 1950 to 2014 from Frederikse et al. (2020). To compute barystatic SLC, Frederikse et al. (2020) summed out mass changes from glaciers, ice sheets, TWS, water impoundment in artificial reservoirs, and groundwater depletion. Frederikse et al. (2020) used an ensemble of GIA estimates, providing a 128,000-member ensemble of predictions, computed by varying solid-Earth parameters (lithosphere thickness and mantle viscosities) and amplitudes of global deglaciation histories over the past 20,000 years. Each ensemble member consistently provided variations in relative sea level, solid-Earth deformation and changes in equivalent water height. These were used to correct GRACE satellite observations. Each ensemble member also comes with a likelihood that reflects how good the fit is to a data set of vertical GNSS velocities and paleo sea-level records.

Most CMIP6 models have "zos" simulations not corrected for the IB effect. For uncorrected models, we estimated IB variations between 1950 and 2014 from sea-level pressure model outputs. The IB variations were calculated following Ponte (2006) equation:

$$\mathrm{IB}(r) = -\frac{P_a - \underline{P_a}}{\rho g} \tag{5}$$

where IB(r) is the inverted barometer contribution to sea level, P_a is the atmospheric pressure at sea level, $\underline{P_a}$ is the global mean ocean surface pressure, approximately 1,013 hPa. The ρ represents the ocean density and g is the gravitational acceleration constant. Similar to barystatic SLC and GRD, the IB(r) values were mapped to TGs locations using the nearest neighbor interpolation considering only ocean grid cells.

3. Methods

Regional analysis was performed following the IPCC AR6 definition of regions (Iturbide et al., 2020). Polar regions and regions that have no coastlines were excluded while the remaining regions were processed further if they include filtered TGs. See Table S2 in Supporting Information S1 for remaining regions while refer to Iturbide et al. (2020) for the rationale definitions and homogeneity analysis. The filtered TGs were located among 23 regions (see Figure 1). The eastern coast of the Atlantic Ocean contained the highest number of TGs (65 TGs). Of these TGs: 41 (N. Europe), 9 (West and Central-Europe), 14 (Mediterranean), and 1 (Sahara). The western coast of the Atlantic Ocean contained 38 TGs: 1 (Greenland), 1 (N. E. North-America), 1 (C. North-America), 32 (E. North-America), 2 (Caribbean), and 2 (S.E. South-America). The eastern coast of the Pacific Ocean contained 30 TGs: 8 (N.W. North-America), 13 (W. North-America), 5 (N. Central-America), 1 (S. Central-America), and 3 (S.W. South-America). The western coast of the Pacific Ocean contained 45 TGs: 2 (Russian-Far-East), 28 (E. Asia), 6 (S.E. Asia), 2 (E. Australia), 4 (S. Australia), and 3 (New Zeeland). South Asia has 4 TGs on the Indian Ocean coastlines.

To represent the regional trend of SLC in regions that have more than one TG, the multivariate technique of Principal Component Analysis (PCA) was performed, relying on TGs data. The PCA aimed to represent all locations in the same region by principal components (PCs) with minimum loss of information. In each region, eigenvalues were plotted against component numbers, and we noticed the percentage of variance. We found that if the eigenvalues remaining after the first principal component (PC1) were less than 1, there is a percentage of variance that exceeds at least 77%. This means the first PC can explain >77% of the variance in the data. Therefore, we considered the PC1 sufficient to explain the total variance, and the PC1 was used to represent the region. Otherwise, we used the average of all TGs to indicate mean regional changes. Further information about PCA can be found in Rencher (2005). Note the results of PCA derived from TGs (i.e., PC1s) were applied to generate regional trends in CM and ESM. The PCA was not performed on the CM and ESM separately.

The research step-wise methodology included three steps. First, we highlighted global hotspots for SLC extremes using two metrics: sea level departures (SLDs) and linear trends. The SLDs were quantified as the departures of annual SLC from the long-term trend, following (Yin, 2023). The long-term linear trend is based on the whole study period (i.e., 1950–2014). Thresholds applied to the standard deviation (σ) were used to delineate extreme departures. We recognize that sea-level extremes are usually studied on local weather-driven time scales (hourly or sub hourly data) and often include contribution by waves, tides, and surge. However, we could not find reliable sea-level observations on a weather time scale over the chosen World regions since 1950. The Global Extreme Sea Level Analysis (GESLA) project might be the biggest high-frequency SLC data set (i.e., hourly and sub-hourly) from 36 international and national data providers (Haigh et al., 2023). However, GESLA data have no special and temporal coverage over the study period and the World reference regions we analyzed in this study (see Figure S4 in Supporting Information S1). Therefore, we identified sea-level decadal extremes using monthly data. Second, we computed the standard deviation of SLC among models to quantify SLC uncertainty in the MEMs. Regions with larger standard deviations were considered to have less fidelity in SLC simulations. Finally, we divided the study period into three intervals: 1950–1970, 1971–1992, and 1993–2014 (Another definition of these intervals is presented in Figures S1–S3 in Supporting Information S1, including periods 1950–1980, 1960–1980, and 1981–2014). Three diagnostics were then used to compare CMs MEM and ESMs MEM with TG observations, and hence assess how well models perform, compared to TGs. These diagnostics are the linear trend, correlation, and the Root Mean Square Error (RMSE). To approximate the uncertainty in the trend of SLC, we implemented the bootstrap sampling bias-corrected and accelerated method with replacement, resampling values 1,000 times. The correlation coefficient was used to compare the temporal trends of observed and simulated SLC. The trend uncertainty, correlation coefficient, and RMSE metrics were used to indicate simulation fidelity and, hence, highlight ambiguous regions as those having large RMSE and low correlation. To make the intercomparison manageable, we compared MEMs with TGs, rather than comparing individual models, aligning with the overall aim of this study. For all diagnostics, the global average was computed as the area-weighted mean.

10.1029/2025EA004402

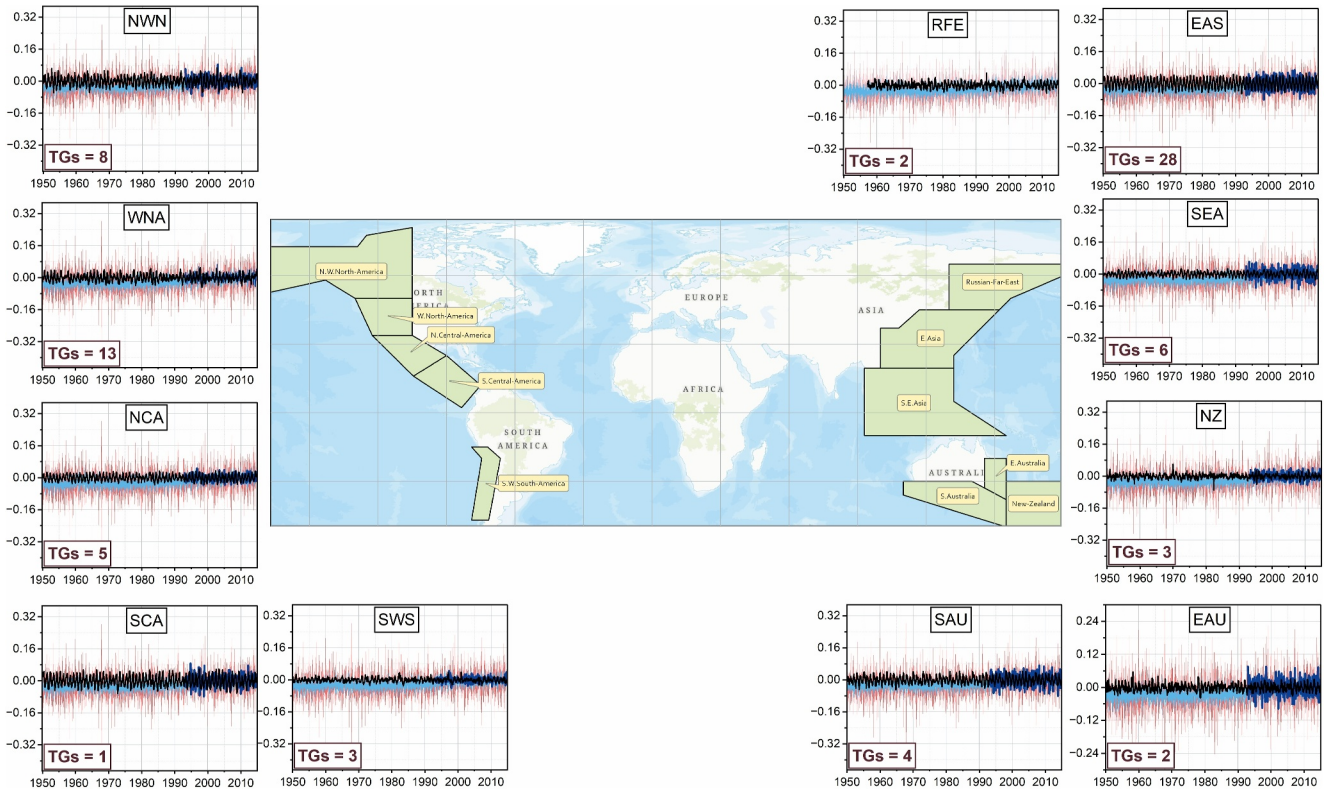

Figure 3. Monthly sea-level change (SLC) as observed by tide gauges (TGs) stations (black line), estimated by satellite altimeters (dark blue line), and simulated by climate models (red lines) and earth system models (light blue lines). The numbers of TGs stations used for calculating regional SLC are shown in the bottom left corners of panels. All panels have identical *y*-axis. Units: m.

4. Results

4.1. Regional Timeseries

Regional time series of SLC from TGs and CMIP6 models is presented in two figures. Figure 3 depicts SLC in 11 reference regions along the Pacific Ocean coastline, while the other 12 regions, which are along the Atlantic and Indian Oceans coastlines, are shown in Figure 4. The CMIP6 simulations generally agree with the TGs timeseries. However, some discrepancy is clear between CMs and ESMs simulations and TGs records where TGs show higher records of SLC compared to CMIP6 models from 1950 to 2014. The models do not correctly represent the trends in most regions. The interannual variations of SLC in CMIP6 models are relatively large in the equatorial Pacific regions that are located between 30°S and 30°N, for example, S. and N. Central-America, N. South-America, and E. and Southeast Asia. The interannual variations of SLC, with TGs, were bigger in CMs compared with ESMs.

Figure 4 shows that ESMs are largely consistent with the simulated trend of SLC with minimal differences compared with CMs. However, models fail to capture SLC represented by TGs in some reference regions. There are large interannual SLC variations in the S. E. South-America, Mediterranean, W.C. Asia, and north Atlantic regions, for example, N. Europe, Greenland, and N. E. North-America. The locations of poorer agreement between SLC observations and CMIP6 simulations include early periods in Greenland, and C. North-America, and W.C. Asia. In some regions, there are substantial variations among the observed inter-annual variability of SLC between regions.

4.2. Sea Level Extremes

We identified global extremes hotspots of SLC as regions where, after removing the long-term linear trend, annual SLDs from TGs exceed three times regional standard deviation (3σ), at least once during the 1950–2014

10.1029/2025EA004402

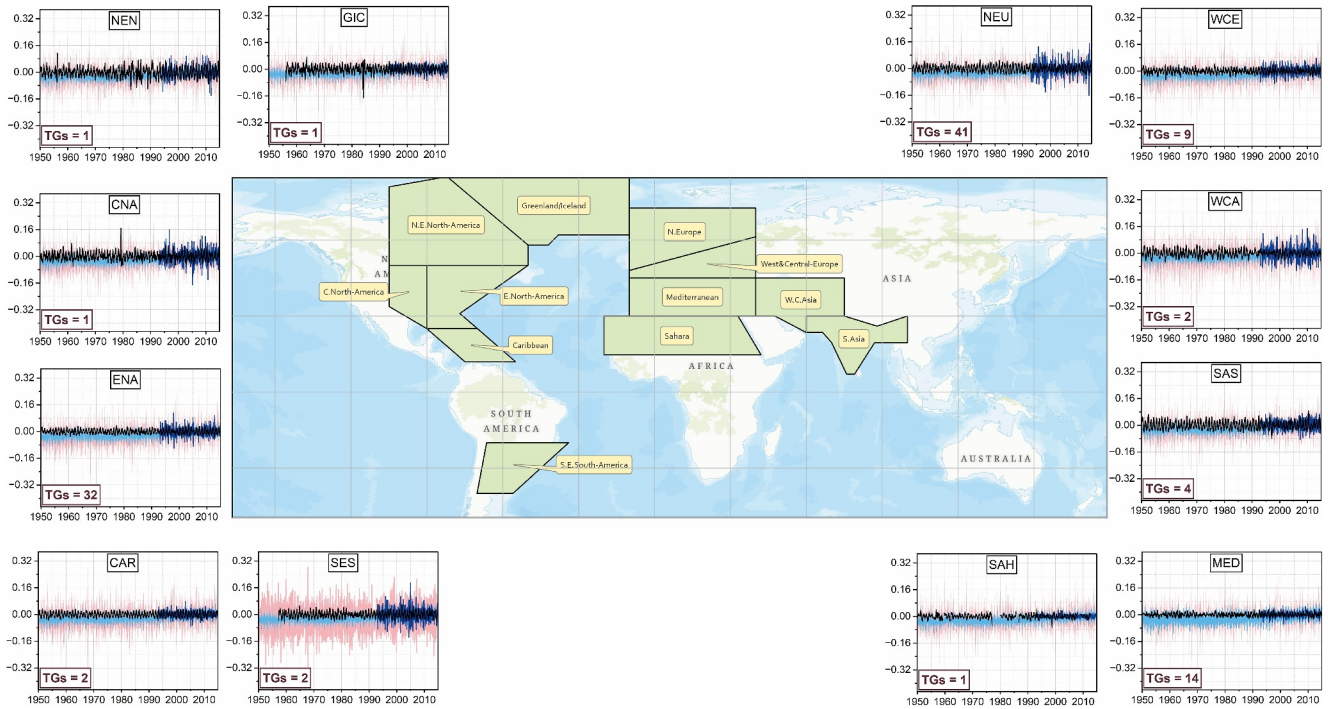

Figure 4. Same as Figure 3 but for regions coasted by the Atlantic and Indian Oceans.

timeframe. Note the 3σ threshold was set as a criterion identifying sea level extremes, following precedent set in Yin (2023); however, we acknowledge that this approach assumes a symmetric Gaussian distribution of SLD with a zero-mean over time, which may not be present in these data.

Figure 5 shows SLD in regions along the coastline of the Pacific Ocean. Four regions satisfied this condition and broke the threshold of a 3σ annual departure. These regions are W. North-America, N. Central-America, S. Central-America, and E. Australia. In W. North-America, the departure of annual sea level spiked in two subsequent years in the 1980s and 1990s. The year 1997 represented the largest departure from the long-term trend line. In N. Central-America, the SLD was maximum in 2014, while before 2014, the departure was not exceeding the 3σ threshold. On the S. Central-America coast, the SLD spikes in 2005. A similar spike (exceeding 3σ) was observed in E. Australia in 2013. Annual SLDs from the long-term linear trends exceeded 2σ only during the last 2 decades in six regions. These regions are S. W. South-America, Russian-Far-East, E. Asia, New-Zealand, N. W. North-America, and S. E. Asia. The SLD exceeded the 2σ threshold once in Russian-Far-East (2014). SLD exceeded the 2σ threshold in E. Asia in all years after 2012, while in the S. Australia region, the single-σ threshold was not broken yet as of 2014.

Figure 6 depicts SLDs in regions along the Atlantic and Indian Oceans. Annual sea levels depart from the 1950–2014 linear trend by 3σ in four regions: Caribbean, West and Central-Europe, S. E. South-America, and the Mediterranean. In the Caribbean, SLDs exceeded 3σ from the long-term trend in three sequent years: 2012–2014. In West and Central-Europe (S. E. South-America), annual SLD broke the 3σ threshold only once (two times). In the Mediterranean, the period after 1995 was unprecedented compared to previous years and the 3σ threshold was broken in 2011. Even though, the SLD had exceeded the single-σ threshold in only one previous year (1970). This means sea level extremes in the mediterranean region were higher during the last 2 decades, compared to previous periods.

4.3. SLC Uncertainty in the MEMs

To assess the fidelity of SLC in the models MEM, the standard deviations of SLC among CMs and ESMs MEMs were calculated. Figure 7 depicts the standard deviations of SLC in the world regions along the coastline of the Pacific Ocean. Models in the ESM ensemble agree with each others on the evolution of SLC better than models in

10.1029/2025EA004402

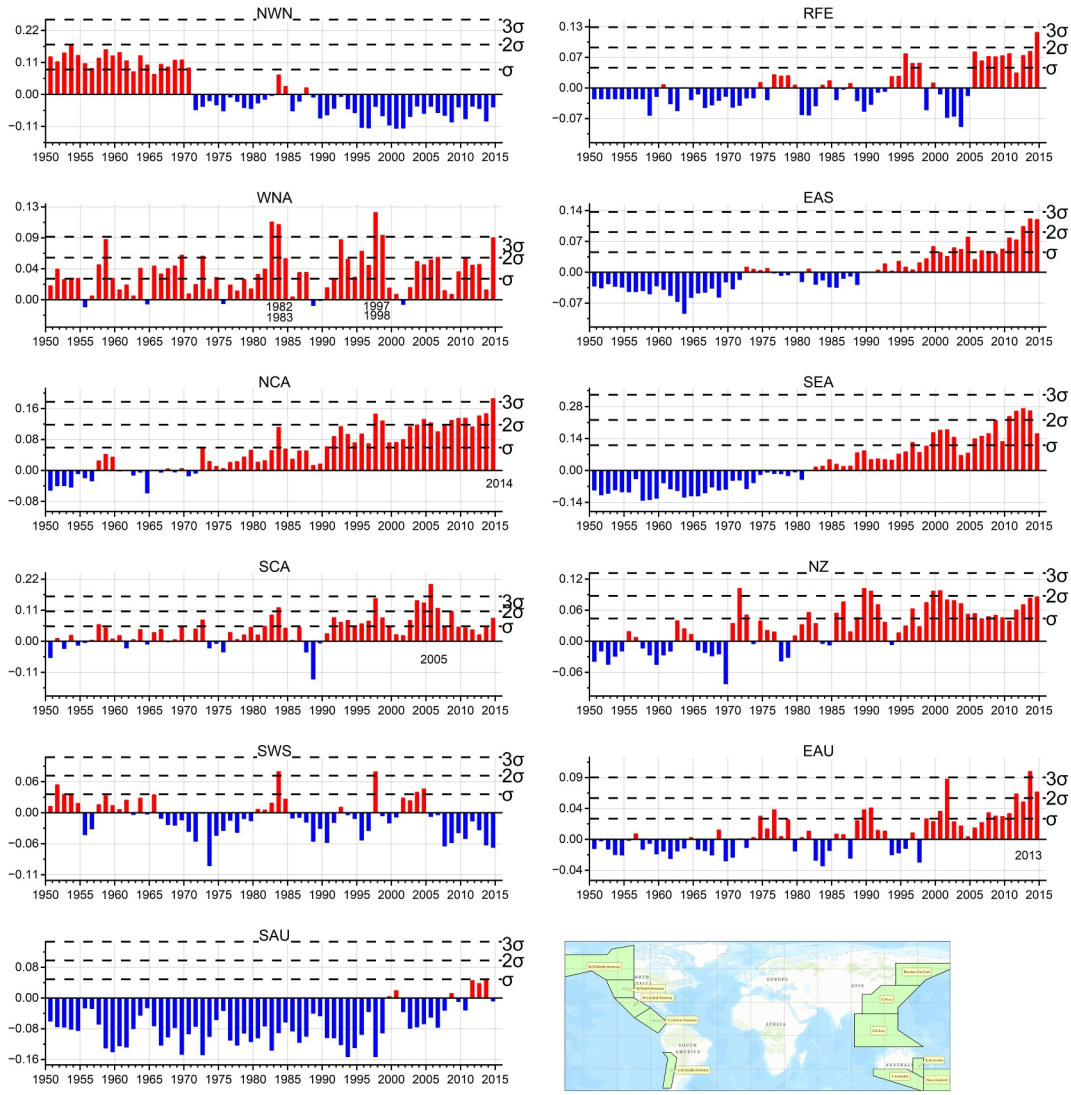

Figure 5. Regional annual sea level departure (SLD) (Units: m) from the long-term linear trends (1950–2014) in regions coasted by the Pacific Ocean. Horizontal lines mark standard deviation (σ) thresholds. Calculations of SLDs are based on tide gauges.

the CM ensemble, with standard deviation does not exceed 0.35 m in most regions, on average. Only in three regions (E. Australia, S. Australia, and S. E. Asia), the standard deviation was high, indicating larger disagreement among the ESM simulations over these regions for these years. Conversely, there is, on average, a larger spread in CM show simulations of SLC. The N. W. North-America, S. Australia, S. E. Asia, and E. Asia had a larger spread among CM models when compared to the other regions. The mean standard deviation was 0.38 m in N. W. North-America, reaching its maximum of 0.45 m in 1965. In S. E. Asia, the mean standard deviation was 0.51 m. The CMs were also less confident on SLC in S. Australia and E. Asia compared to other regions (mean = 0.30 and 0.35 m, respectively).

The standard deviation of SLC among CMs and ESMs in other regions that are along the coast of the Atlantic and Indian Oceans, is shown in Figure 8. The CMs show low fidelity on SLC over most regions, compared with ESMs, especially in W. C. Asia, the Mediterranean, and N. Europe. In N. Europe, a large spread is found in the model ensembles with a mean standard deviation of 1.0 m in CMs while 0.23 m in ESMs. The standard deviation among CMs reached a high value in W. C. Asia (i.e., 4.2 m). In N. E. North-America, the mean standard deviation was 0.33 m in CMs but 0.27 m in ESMs. Maximum values of standard deviation in N. E. North-America were

10.1029/2025EA004402

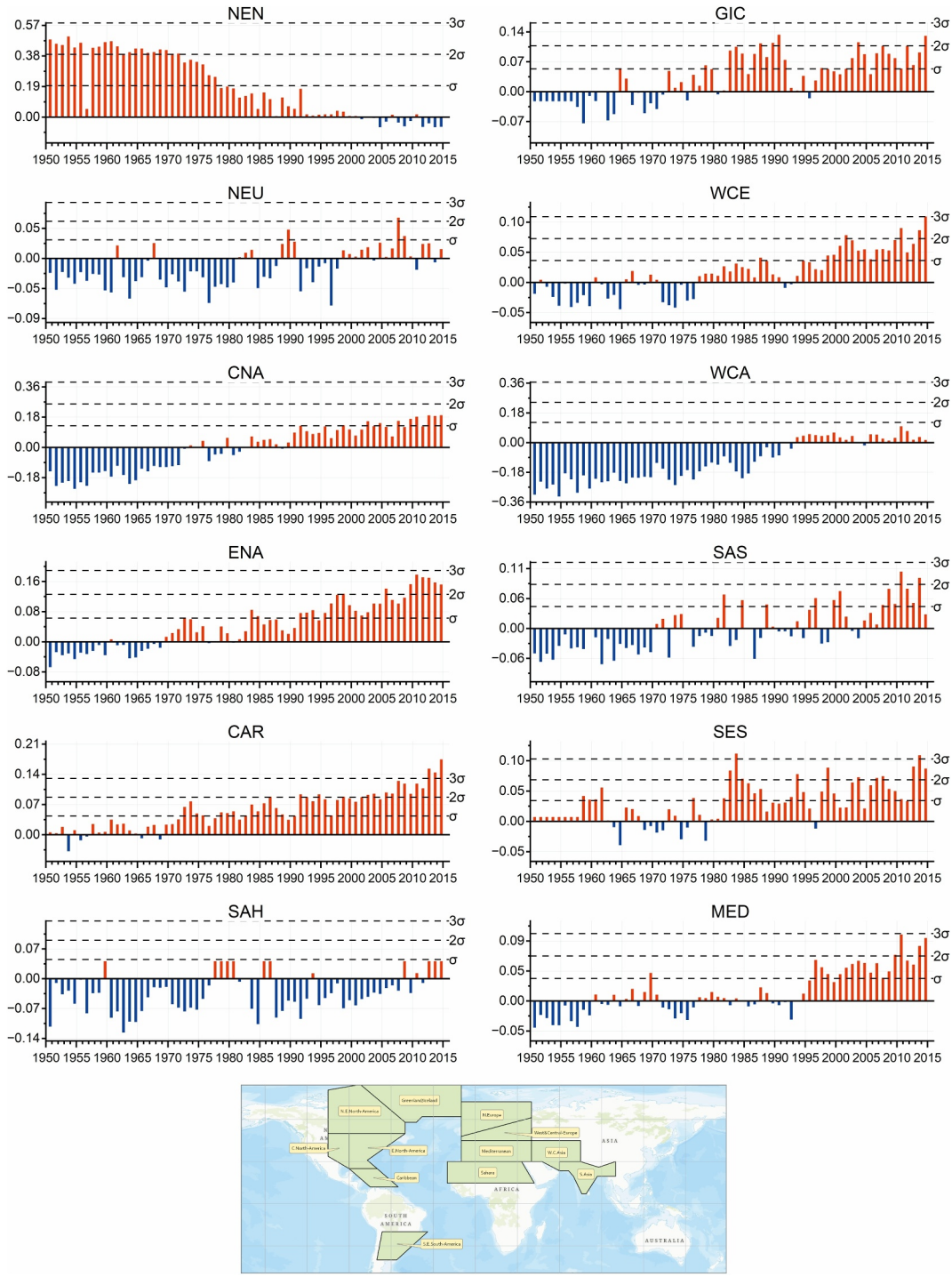

Figure 6. Same as Figure 5 but other regions coasted by the Atlantic and Indian Ocean.

observed in 2003. In E. North-America, CMs (ESMs) models had a mean standard deviation of ∼0.25 m. The inconsistency among CMIP6 models may arise due to differences in model inputs and physics, initial conditions, parameterizations, and representation of natural variability (Fox-Kemper et al., 2021).

10.1029/2025EA004402

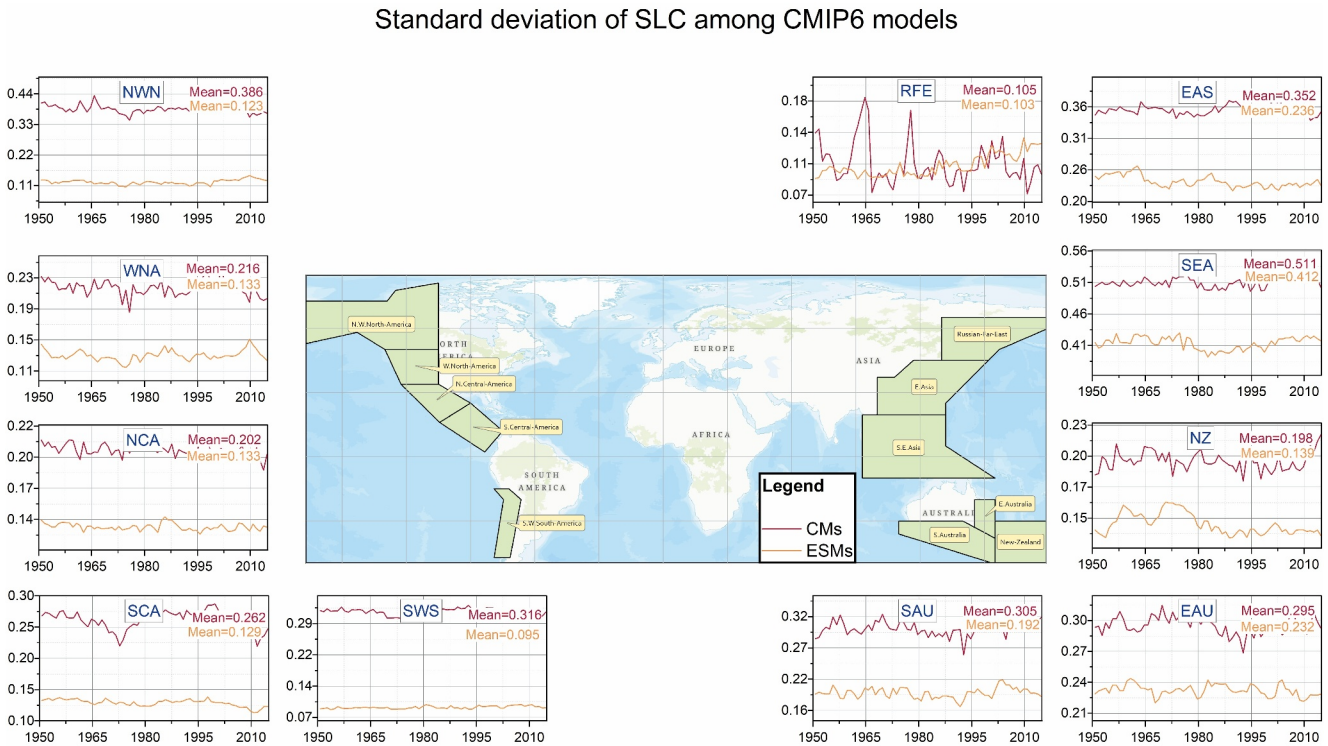

Figure 7. Regional standard deviation of sea-level change among climate models and earth system models during 1950–2014 in the Intergovernmental Panel on Climate Change AR6 regions along the coastline of the Pacific Ocean. Mean values of standard deviation are in the top right corners. Units: m.

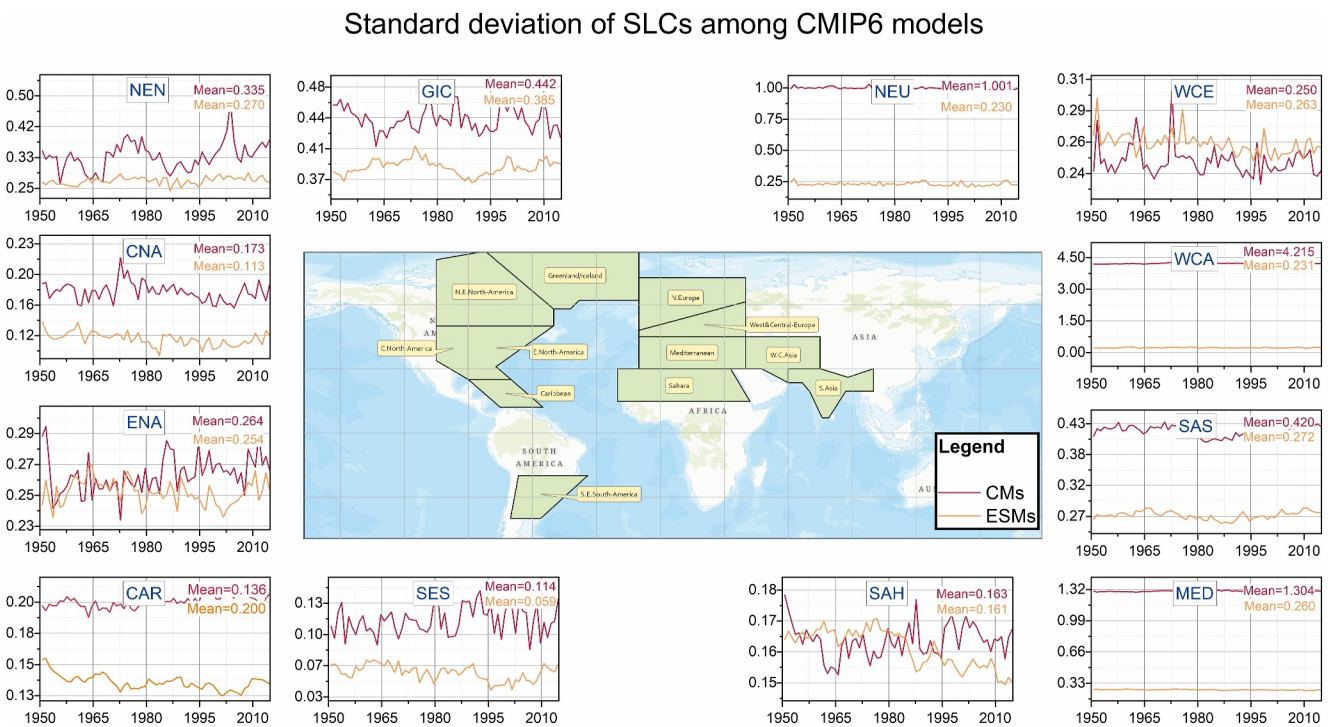

Figure 8. Same as Figure 7 but for regions that are along the coastline of the Atlantic and Indian Oceans.

10.1029/2025EA004402

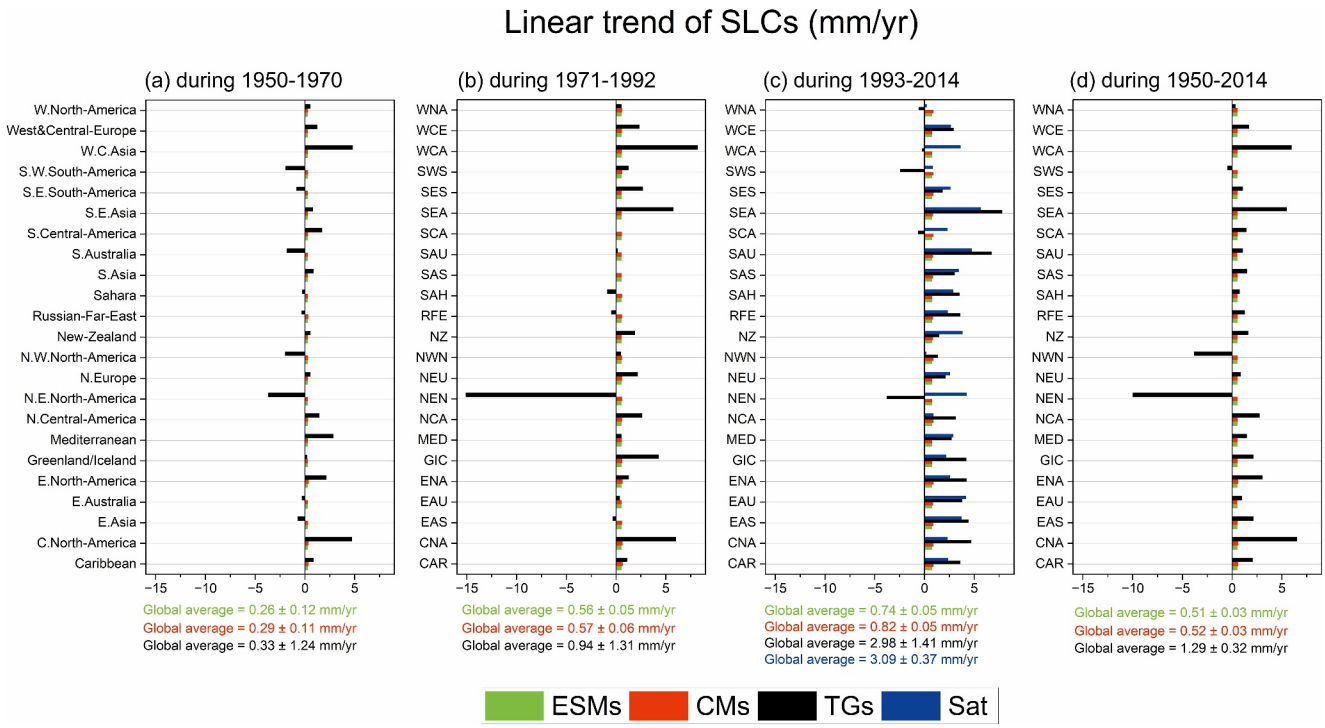

Figure 9. The linear trend of regional sea-level change in tide gauges and climate models and earth system models MEMs. Columns show values during (a) 1950–1970, (b) 1971–1992, and (c) 1993–2014. Whereas column (d) shows values during the whole study period.

4.4. Comparison Between CMIP6 and TGs

The confidence of CMs and ESMs MEMs on SLC that we noticed in Figures 7 and 8 may not mean the reliability of models' simulations. Therefore, we examined the reliability of CMIP6 simulations through a comparison with TGs observations. Figure 9 compares the linear trends of SLC in TGs, CMs and ESMs during four periods: 1950–

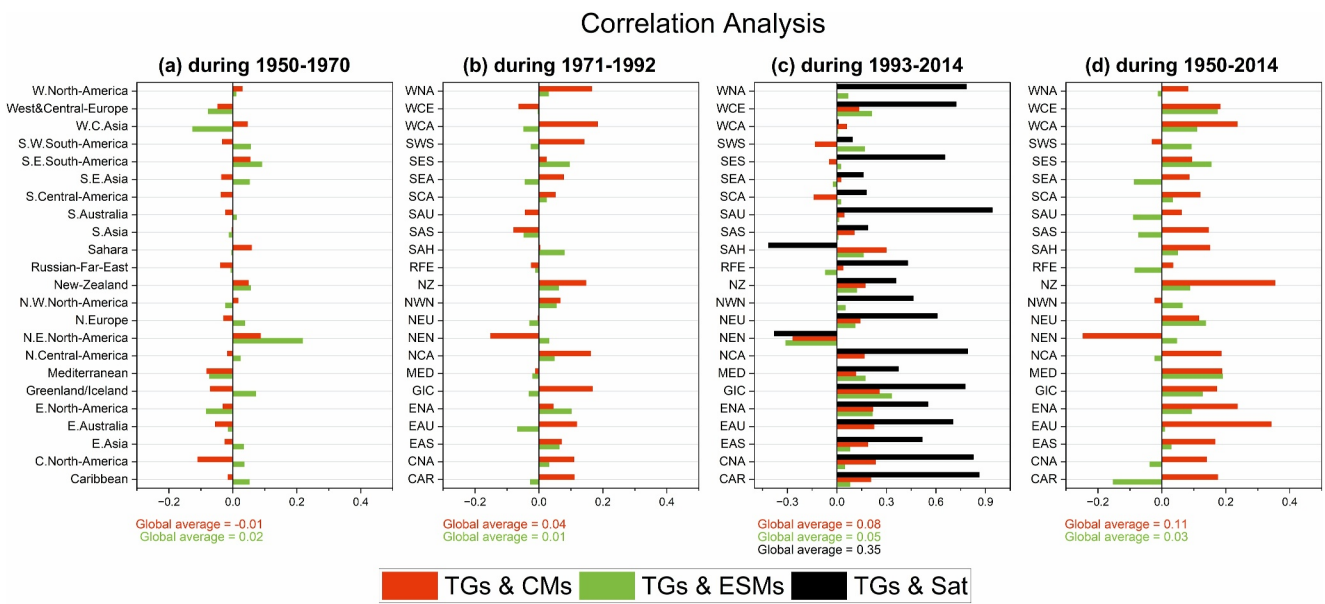

Figure 10. Same as Figure 9 but for trend correlation between tide gauges and climate models and earth system models MEMs.

10.1029/2025EA004402

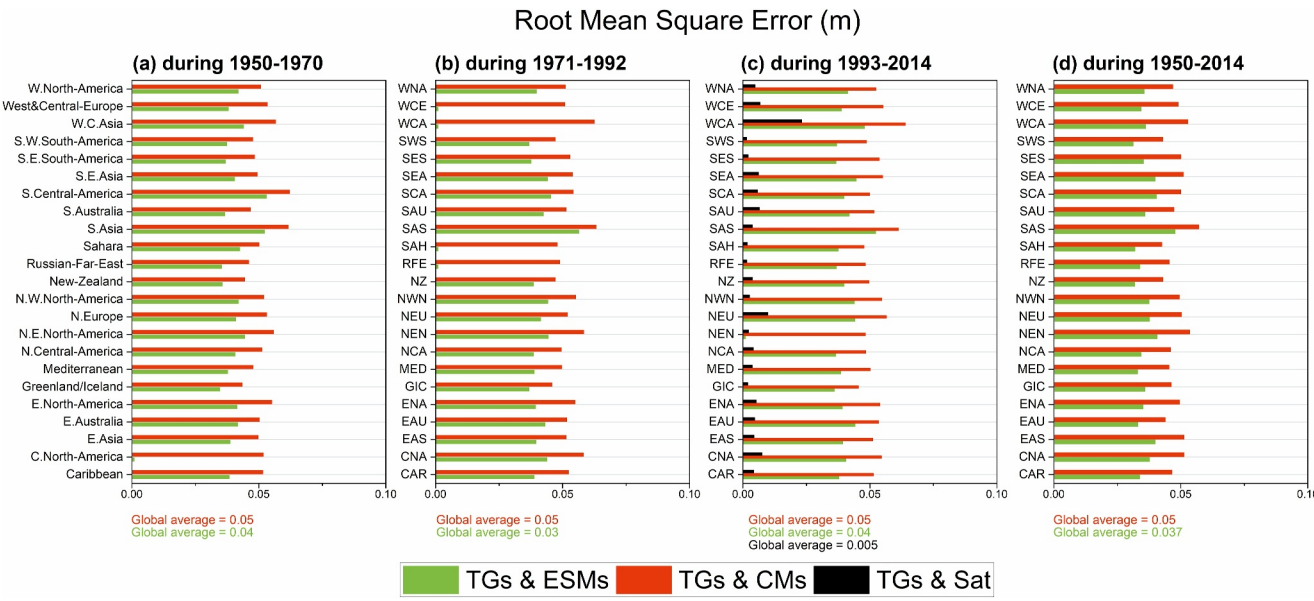

Figure 11. Same as Figure 9 but for the Root Mean Square Error.

1970, 1971–1992, 1993–2014, and 1950–2014. Whereas Figures 10 and 11 compare the correlation and RMSE between CMs MEM and ESMs MEM, and TGs observations.

Sea level is generally increasing with time in TGs and CMIP6 models, with an intensification that is unequivocal among regions, as Figure 9 shows. Regarding TGs, the global weighted-average increased from 0.33 ± 1.24 mm/yr during 1950–1970 to 0.94 ± 1.31 mm/yr during 1971–1992 and 2.98 ± 1.41 mm/yr during the satellite era. During the whole analyzed period (1950–2014), SLC intensified by an average rate of 1.29 ± 0.32 mm/yr in TGs. It varied between −9.98 ± 0.34 mm/yr in N. E. North-America to 6.52 ± 0.26 mm/yr in C. North-America. Agreement is evident between satellite and TGs trends during 1993–2014 as satellite reported a similar trend of 3 ± 0.37 mm/yr. Five regions display rapid increasing rates that were +100% over the global mean (hereafter known as hotspots). These hotspots are C. North-America (6.52 ± 0.26 mm/yr), S.E. Asia (5.49 ± 0.48 mm/yr), W.C. Asia (5.97 ± 0.38 mm/yr), E. North-America (3.03 ± 0.23 mm/yr), and N. Central-America (2.76 ± 0.24 mm/yr). Together these regions constitute 26% of the total analyzed area. The trend of SLC was above the global average in three other regions: Caribbean, E. Asia, and Greenland. In N. W. North-America, the sea level was decreasing at a rate of −3.85 ± 0.56 mm/yr, while most other regions had an increasing trend of SLC that did not exceed the global average.

The CMIP6 simulations, generally, confirm the observed increasing trend of sea level in TGs but with some differences (mostly mean systematic underestimation) along coasts. While TGs reported a global average SLC of 1.29 ± 0.32 mm/yr during 1950–2014, the trend was ∼0.5 ± 0.03 mm/yr in CMs and ESMs MEMs. During 1950–1970, TGs reported a trend of 0.33 ± 1.42 mm/yr, while CMs and ESMs simulated a trend of 0.29 ± 0.11 and 0.26 ± 0.12 mm/yr, respectively. Similar inconsistency can be noticed during 1971–1992 and 1993–2014 periods where TGs reported higher global average than CMs and ESMs simulate. Inconsistencies between CMIP6 models and observations are evident at regional scale, as well. During 1950–2014, N. E. North-America had a decreasing trend of −9.98 mm/yr from TGs. Whereas CMs and ESMs reported increasing trends of 0.51 mm/yr. Similarly, in C. North-America, TGs reported an increasing trend of 6.52 mm/yr during 1950–2014, while CMs and ESMs MEMs simulated under related trends of 0.59 and 0.51 mm/yr, respectively.

To define uncertain regions of sea-level simulations, we calculated the correlation coefficient and RMSE between observations and CMIP6 models. Figure 10 shows the correlation between TGs, and CMs and ESMs MEMs during 1950–1970, 1971–1992, 1993–2014, and 1950–2014. It also shows correlations between TGs observations and satellite estimates during 1993–2014. There was a strong correlation between TGs and satellite estimates. It exceeded 0.7 in eight regions, hitting 0.94 in S. Australia, 0.86 in Caribbean, 0.82 in C. North-America, and 0.78 in W. North-America. Most other regions had a correlation that exceeded 0.5. However, some regions have a low

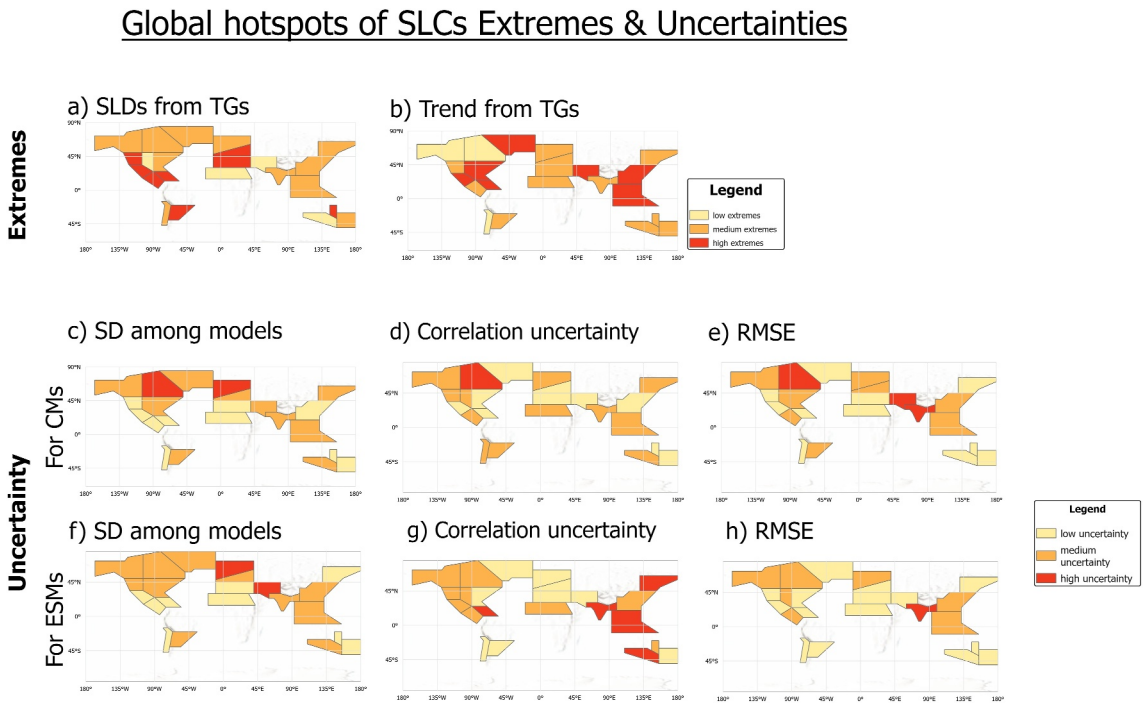

Figure 12. (a, b) Global hotspots for sea level extremes, (c–e) uncertainties from climate models, and (f–h) earth system models during 1950 and 2014, over the analyzed regions.

correlation between satellite records and TGs observations, reaching <0.2 in S. Central-America, S. Asia, S. E. Asia, S. W. South-America, and W. C. Asia. Negative correlation was found in two regions: N. E. North-America (−0.37) and Sahara (−0.41). This might be attributed to the misrepresentation of more localized-scale VLM data over these regions as well as possible errors resulting from interpolating satellite data. The representation of VLM data might be satisfying in other regions since correlation was strong. Regarding CMIP6 models, the CMs have better correlation with TGs on average, if compared with ESMs. During 1950–2014, the correlation coefficient between TGs and CMs had a global average of 0.11. On the other hand, the correlation between ESMs and TGs was only 0.03.

Figure 11 depicts the RMSE values between different data sets. Except with satellite data where RMSE was very small, the global weighted average RMSE between TGs, and CMs and ESMs varied between 0.04 and 0.05 m, with little differences among periods. Regions with large RMSE between TGs and CMs are mostly identical to those that have low correlations. The CMIP6 historical simulations over these regions have higher uncertainty, thus diminishing the reliability of their sea level simulations.

5. Summary and Discussion

Hundreds of millions of people live in coastal low-lying areas and face a growing frequency and severity of coastal flooding due to SLC every year (Kulp & Strauss, 2019; Nicholls et al., 2021). The global trend of MSL, described in previous literature, is inadequate to explain the rapid acceleration in some regions. Therefore, a detailed analysis of sea level extremes and uncertainty, over the IPCC reference regions as this study presented, is required. Figure 12 summarized the research results. It depicts global hotspots of sea level extremes and uncertainties during the whole period. Extreme hotspots were defined as regions where SLD and trend estimations from TGs are the highest (Figures 12a and 12b). Whereas uncertain regions are defined based on three categories: standard deviation among models (Figures 12c and 12f), correlation between the TGs observations and MEM (Figures 12d and 12g), and RMSE between TGs observations and MEM (Figures 12e and 12h).

Global hotspots for sea level extremes are shown in Figures 12a and 12b. In Figure 12a, if SLDs exceeded 3σ (2σ), extremes were considered high (medium). Otherwise, extremes were considered "low." Identical hotspots for

SLD included regions that are mainly located in North and Central America, Mediterranean, West and Central-Europe, and E. Australia. Regarding trend analysis (Figure 12b), we considered regions that had an intensification exceeding two times the global average of 1.29 ± 0.32 mm/yr as high extremes regions. Around 26% of the regions included in this study satisfied this condition having a SLC > 2.6 mm/yr. These regions are E. and C. North-America, N. Central-America, W. C. Asia, and S. E. Asia. Extremes analysis shows that the distribution of intensification is unequivocally superimposing potential influence of internal climate variability and other local anthropogenic factors. In some regions, for example, E. North-America, high-end SLC (extremes) coincide with record-breaking hurricanes. These Hurricanes caused storm surges of 70–210 cm at TGs locations (Yin, 2023), meaning that the sea level extremes had intensified hurricane storm surges and increased flood damage cost. These extremes alarm hotspots regions that SLC adaptation measures are crucial to preserving current aims of coastal flood protection. Note regional trends in C. North-America, E. North-America, and N. Central-America agree with literature that reported similar increasing trends of SLC but used other sources of data. For instance, Yin (2023) used NOAA Tides and Currents and found SLC rates that exceed 10 mm/yr in the U.S. Southeast and Gulf Coasts. Some stations recorded similar trends in our analysis. Sallenger et al. (2012) concluded the northeastern U.S. coast was a SLC hotspot region, during 1950–2009, with a SLC rate that exceeded the global average. Wdowinski et al. (2016) also detected a decadal SLC rate from 3 ± 2 mm/yr before 2006 to 9 ± 4 mm/yr after 2006. Sweet et al. (2021) defined the southeastern U.S. and Gulf coasts as SLC hot spots, which experienced an extra 400%–1,100% increase in high tide floods in 2020, compared to 2000 (Sweet et al., 2021). For uncertainty, both CMs and ESMs share similar hotspots, with highly uncertain regions that include subtropical North Atlantic regions and W. Central Asia.

While the trend observed by TGs in W. C. Asia was 8.21 mm/yr during 1971–1992, it decreased to −0.25 mm/yr during 1993–2014. During the whole period, the trend was 5.97 mm/yr. In E. North-America, the SLC observed from TGs was 2.17 mm/yr during 1950–1970 and 1.27 mm/yr during 1971–1992 but 4.12 mm/yr during 1993–2014. We repeated the trend analysis, correlation coefficient, and RMSE using different definitions of periods. This time, we considered different periods of 1950–1980, 1960–1980, and 1981–2014. Results are presented in Figures S1–S3 in Supporting Information S1. The analysis reveals that TGs rates during the defined periods (1950–1970, 1971–1992, and 1993–2014) may not be directly comparable with each other or with the full period between 1950 and 2014. It can be concluded that the variations in sea level trends over periods might be related to the reason that coastal and estuarine environments are highly dynamic with several factors that might cause regional differences in sea levels. These factors include VLM, Earth gravitational changes, ocean dynamics, and rotation and deformation due to land ice and land-water changes (Fox-Kemper et al., 2021; Slangen et al., 2017).

Additional work can follow this study to improve regional sea level simulations in uncertain regions. The VLM calculation might be incorrect in regions where VLM depends heavily on active tectonic movement and anthropogenic activities (groundwater and gas extraction). As the IPCC AR6 reports stated, there is low to medium confidence in the VLM projections, depending on locations. Local accurate VLM assessments can lead to more accurate SLC simulations. Uncertain regions could also utilize dynamic downscaling of Global Climate Models (GCMs) using higher resolution atmospheric and oceanic models to resolve local changes in sea levels and reduce (or statistically bias-correct) mean-state biases in CMIP6 models. Even though most CMIP6 models reproduce the observed mean state of the DSL reasonably well, previous literature (Lyu et al., 2020; Sajidh & Chatterjee, 2023) reported consistent mean states bias, when compared with observations. Dynamic downscaling requires getting boundary conditions from higher resolution GCMs. Despite the high cost associated with such computation, higher resolution can lead to better representation of SLC, especially in coastal areas with small-scale tidal processes and bathymetric features (Y. Jin et al., 2021; Sannino et al., 2022). An overarching question involving these extremes is how much they can even be attributed to forced modes of climate change and other deterministic factors (e.g., VLM, GRD) versus (mostly ocean dynamic) internal sea level variability, the latter being unlikely to match between observations and GCMs or ESMs in any case (which is why we use multi-model mean and long term trends here) and at any resolution (e.g., Cheung et al., 2025). Further research can also disclose the relationship between increasing rate of SLC and climatic parameters such as wind and atmospheric pressure anomalies (Yin, 2023). Besides, although challenging due to the inherent complexity and multi-scale nature of the climate system, a complete removal of natural variability from CMIP6 models is necessary for a better understanding of the evolution of sea levels. Neither step could provide a complete improvement alone, but incorporating all these steps can eliminate uncertainty in SLC.

5.1. Dynamics Underpin Regional SLC

Recent progress in CMIP6 models included using physically based emulators to confirm sea level projections consistency with the AR6-assessed Equilibrium Climate Sensitivity and global surface air temperature. It also included significant improvement in the ocean model resolution. This led to an overall agreement between sea level simulations in CMIP6 models and TGs observations that improved with time but still suffer in some regions. TGs show a rapid SLC that exceeds what CMIP6 models simulate in most analyzed regions. Some uncertain regions are apparent in Figure 12 where the correlation between TGs observations and CMIP6 models is low while the RMSE is high. TGs records were corrected for the VLM processes and comparison between TGs and satellite estimates were good. Therefore, the inconsistencies between TGs observations and CMIP6 models have not totally arisen from VLM estimates; it also arose from climatic variability and other local factors, for example, ocean dynamic, human activities.

Several studies attributed SLC to the storage of heat by oceans (Gregory et al., 2016; Smeed et al., 2018; Wilson et al., 2016), estimating that ocean warming accounts for more than 1/3 of the global-mean SLC through thermal expansion, and thus dominates regional changes in SLC. Observations revealed that the ocean heat content encounters distinct spatial variability (Cheng et al., 2022; Fox-Kemper et al., 2021). The Pacific Ocean is projected to be the largest heat reservoir considering its size. However, the IPCC AR6 concluded a larger SLC in the Western Pacific than in the Eastern Pacific during 1993–2018 (Fox-Kemper et al., 2021). Observations also showed the Pacific Ocean area-averaged warming resembled the global mean and was not to be the strongest, compared with the Atlantic and southern oceans, during 1958 and 2019 (Cheng et al., 2022). The Mediterranean Sea area-averaged warming is observed to exceed all rates of the Pacific, Indian, and Southern Oceans (Cheng et al., 2022). However, this study emphasizes previous findings and highlights regional differences showing some hotspots in the Pacific, Atlantic, and Indian Oceans where SLC exceeded the Mediterranean during 1950–2014, for example, E. and C. North-America, N. Central-America, W. C. Asia, and S. E. Asia. Bronselaer and Zanna (2020) aimed to understand the mechanisms that govern ocean heat redistribution at regional scales, impacting SLC. They found that, in the Atlantic Ocean (40°S–40°N) and eastern tropical Pacific Ocean, the increase in regional SLC is attributed to the warming resulting from redistribution which is often dominated by internal variability, which may exceed the impact of added heat storage (where forced ocean dynamic change tends to dominate) in the fixed-circulation by >300%. Bronselaer and Zanna (2020) also found the changes in ocean circulation might have probably cooled the subtropical gyres in the Indian and Pacific Oceans, decreasing regional SLC. We believe there are still many complexities in projecting SLC changes and accounting for internal variability, which should be considered when analyzing and interpreting SLC changes in atmospheric and environmental sciences. Apart from heat and carbon storage interpretations, another reason behind spatiotemporal variability of SLC might be the present.

6. Conclusion

To make effective decisions for SLC adaptation, one should depend on reliable future projections. However, reliable future projections of SLC are still unfeasible from CMIP6 simulations since, as this study showed, historical simulations are inaccurate in some regions not to mention the uncertainty associated with ice sheets contributions and future human activities. This highlights our need for some other effective ways to produce reliable future projections. Our analysis highlighted hotspots regions of sea level extremes and uncertainty, for example, subtropical North Atlantic regions and W. Central Asia. Getting a better understanding of the physical processes controlling SLC in these regions can lead to more physically based simulations with more representative ensembles, allowing to capture extremes and narrow uncertainties. Such advancement would help improve models' confidence, enabling policymakers, coastal planners, and stakeholders to make informed decisions as robust SLC adaptation strategies depend heavily on realistic simulations. Furthermore, extreme hotspots alarm regions where even minor storm surges can inundate coastal low-lying areas, displacing communities and causing extensive damage to infrastructure. On the other hand, uncertain hotspots alarm researchers and decision-makers to interpret the results in the context of a broader range of projections to better count for the potential range of future SLC scenarios.

Conflict of Interest

The authors declare no conflicts of interest relevant to this study.

Data Availability Statement

TGs observations are available from the Permanent Service for Mean Sea Level (PSMSL) https://www.psmsl.org/. Satellite altimeter estimates of gridded sea level anomalies are available at the ECMWF Copernicus Marine Service https://marine.copernicus.eu/access-data. The CMIP6 simulations are accessed at the Earth System Grid Federation (ESGF) website (https://esgf-node.llnl.gov/projects/cmip6/).

Acknowledgments
We thank the CMIP6 climate modeling groups for producing model output; the Earth System Grid Federation (ESGF) for archiving and making available CMIP6 models' data; and the ECMWF Copernicus Marine Service for making available satellite gridded sea levels. This work was supported in part by the National Science Foundation under RII Track-2 FEC Award 2316271, Community-Driven Coastal Climate Research & Solutions for the Resilience of New England Coastal Populations (www.3crs.org), and by the National Oceanic and Atmospheric Administration through the Georgia Coastal Resilience Hub (www.cearhub.org). The authors gratefully acknowledge the support of these programs in advancing applied coastal resilience research.

References

Bronselaer, B., & Zanna, L. (2020). Heat and carbon coupling reveals ocean warming due to circulation changes. *Nature*, *584*(7820), 227–233. https://doi.org/10.1038/s41586-020-2573-5

Bulgin, C. E., Mecking, J. V., Harvey, B. J., Jevrejeva, S., McCarroll, N. F., Merchant, C. J., & Sinha, B. (2023). Dynamic sea-level changes and potential implications for storm surges in the UK: A storylines perspective. *Environmental Research Letters*, *18*(4), 044033. https://doi.org/10.1088/1748-9326/acc6df

Chen, H., He, Z., Xie, Q., & Zhuang, W. (2023). Performance of CMIP6 models in simulating the dynamic sea level: Mean and interannual variance. *Atmospheric and Oceanic Science Letters*, *16*(1), 100288. https://doi.org/10.1016/j.aosl.2022.100288

Cheng, L., von Schuckmann, K., Abraham, J. P., Trenberth, K. E., Mann, M. E., Zanna, L., et al. (2022). Past and future ocean warming. *Nature Reviews Earth & Environment*, *3*(11), 776–794. https://doi.org/10.1038/s43017-022-00345-1

Cheung, A. H., Sane, A., & Fox-Kemper, B. (2025). Understanding the characteristics and drivers of Pacific decadal variability over the last millennium. *Climate Dynamics*. (preprint). https://doi.org/10.21203/rs.3.rs-6164076/v2

CMEMS. (2018). Sea level gridded data from satellite observations for the global ocean from 1993 to present. *Copernicus Climate Change Service (C3S) Climate Data Store (CDS)*. https://doi.org/10.24381/cds.4c328c78

Deepa, J. S., Gnanaseelan, C., & Parekh, A. (2021). The sea level variability and its projections over the Indo-Pacific Ocean in CMIP5 models. *Climate Dynamics*, *57*(1–2), 173–193. https://doi.org/10.1007/s00382-021-05701-3

Ferrero, B., Tonelli, M., Marcello, F., & Wainer, I. (2021). Long-term regional dynamic Sea Level changes from CMIP6 projections. *Advances in Atmospheric Sciences*, *38*(2), 157–167. https://doi.org/10.1007/s00376-020-0178-4

Fox-Kemper, B. H. T. H., Xiao, C., Aðalgeirsdóttir, G., Drijfhout, S. S., Edwards, T. L., Golledge, N. R., et al. (2021). Ocean, Cryosphere and Sea Level change. In V. Masson-Delmotte, P. Zhai, A. Pirani, S. L. Connors, C. Péan, S. Berger, et al. (Eds.), *Climate change 2021 – The physical science basis: Working group I contribution to the sixth assessment report of the intergovernmental panel on climate change* (pp. 1211–1362). Cambridge University Press. https://doi.org/10.1017/9781009157896.011

Frederikse, T., Landerer, F., Caron, L., Adhikari, S., Parkes, D., Humphrey, V. W., et al. (2020). The causes of sea-level rise since 1900. *Nature*, *584*(7821), 393–397. https://doi.org/10.1038/s41586-020-2591-3

Gregory, J. M., Bouttes, N., Griffies, S. M., Haak, H., Hurlin, W. J., Jungclaus, J., et al. (2016). The Flux-Anomaly-Forced Model Intercomparison Project (FAFMIP) contribution to CMIP6: Investigation of sea-level and ocean climate change in response to CO_2 forcing. *Geoscientific Model Development*, *9*(11), 3993–4017. https://doi.org/10.5194/gmd-9-3993-2016

Gregory, J. M., Griffies, S. M., Hughes, C. W., Lowe, J. A., Church, J. A., Fukimori, I., et al. (2019). Concepts and terminology for sea level: Mean, variability and change, both local and global. *Surveys in Geophysics*, *40*(6), 1251–1289. https://doi.org/10.1007/s10712-019-09525-z

Haigh, I. D., Marcos, M., Talke, S. A., Woodworth, P. L., Hunter, J. R., Hague, B. S., et al. (2023). GESLA version 3: A major update to the global higher-frequency sea-level dataset. *Geoscience Data Journal*, *10*(3), 293–314. https://doi.org/10.1002/gdj3.174

Hammond, W. C., Blewitt, G., & Kreemer, C. (2016). GPS imaging of vertical land motion in California and Nevada: Implications for Sierra Nevada uplift. *Journal of Geophysical Research: Solid Earth*, *121*(10), 7681–7703. https://doi.org/10.1002/2016JB013458

Hammond, W. C., Blewitt, G., Kreemer, C., & Nerem, R. S. (2021). GPS imaging of global vertical land motion for studies of sea level rise. *Journal of Geophysical Research: Solid Earth*, *126*(7), 2021–022355. https://doi.org/10.1029/2021jb022355

Holgate, S. J., Matthews, A., Woodworth, P. L., Rickards, L. J., Tamisiea, M. E., Bradshaw, E., et al. (2013). New data systems and products at the permanent service for mean sea level. *Journal of Coastal Research*, *29*(3), 493–504. https://doi.org/10.2112/JCOASTRES-D-12-00175.1

Iturbide, M., Gutiérrez, J. M., Alves, L. M., Bedia, J., Cerezo-Mota, R., Cimadevilla, E., et al. (2020). An update of IPCC climate reference regions for subcontinental analysis of climate model data: Definition and aggregated datasets. *Earth System Science Data*, *12*(4), 2959–2970. https://doi.org/10.5194/essd-12-2959-2020

Jesse, F., Le Bars, D., & Drijfhout, S. (2024). Processes explaining increased ocean dynamic sea level in the North Sea in CMIP6. *Environmental Research Letters*, *19*(4), 044060. https://doi.org/10.1088/1748-9326/ad33d4

Jevrejeva, S., Williams, J., Vousdoukas, M. I., & Jackson, L. P. (2023). Future sea level rise dominates changes in worst case extreme sea levels along the global coastline by 2100. *Environmental Research Letters*, *18*(2), 024037. https://doi.org/10.1088/1748-9326/acb504

Jin, C., Liu, H., & Lin, P. (2023). Evaluation of the seasonal to decadal variability in dynamic sea level simulations from CMIP5 to CMIP6. *Geoscience Letters*, *10*(1), 35. https://doi.org/10.1186/s40562-023-00291-w

Jin, C., Liu, H., Lin, P., & Li, Y. (2024). Uncertainties in the projection of dynamic sea level in CMIP6 and FGOALS-g3 large ensemble. *Journal of Climate*, *37*(6), 1919–1935. https://doi.org/10.1175/JCLI-D-23-0272.1

Jin, Y., Köhl, A., Jungclaus, J., & Stammer, D. (2023). Mechanisms of projected sea-level trends and variability in the southeast Asia region based on MPI-ESM-ER. *Climate Dynamics*, *62*(2), 973–988. https://doi.org/10.1007/s00382-023-06960-y

Jin, Y., Zhang, X., Church, J. A., & Bao, X. (2021). Projected sea-level changes in the marginal seas near China based on dynamical downscaling. *Journal of Climate*, *34*(17), 1–52. https://doi.org/10.1175/jcli-d-20-0796.1

Kopp, R. E., Oppenheimer, M., O'Reilly, J. L., Drijfhout, S. S., Edwards, T. L., Fox-Kemper, B., et al. (2023). Communicating future sea-level rise uncertainty and ambiguity to assessment users. *Nature Climate Change*, *13*(7), 648–660. https://doi.org/10.1038/s41558-023-01691-8

Kulp, S. A., & Strauss, B. H. (2019). New elevation data triple estimates of global vulnerability to sea-level rise and coastal flooding. *Nature Communications*, *10*(1), 4844. https://doi.org/10.1038/s41467-019-12808-z

Lee, J.-Y., Marotzke, J., Bala, G., Cao, L., Corti, S., Dunne, J. P., et al. (2021). Future global climate: Scenario-based projections and near-term information. In *Climate change 2021: The physical science basis. Contribution of working group I to the sixth assessment report of the intergovernmental panel on climate change* (pp. 553–672). Cambridge University Press.

Lyu, K., Zhang, X., & Church, J. A. (2020). Regional dynamic Sea Level simulated in the CMIP5 and CMIP6 models: Mean biases, future projections, and their linkages. *Journal of Climate*, *33*(15), 6377–6398. https://doi.org/10.1175/jcli-d-19-1029.1

Meyssignac, B., Slangen, A. B. A., Melet, A., Church, J. A., Fettweis, X., Marzeion, B., et al. (2017). Evaluating model simulations of twentieth-century sea-level rise. Part II: Regional sea-level changes. *Journal of Climate*, *30*(21), 8565–8593. https://doi.org/10.1175/jcli-d-17-0112.1

Nicholls, R. J., Lincke, D., Hinkel, J., Brown, S., Vafeidis, A. T., Meyssignac, B., et al. (2021). A global analysis of subsidence, relative sea-level change and coastal flood exposure. *Nature Climate Change*, *11*(4), 338–342. https://doi.org/10.1038/s41558-021-00993-z

Palmer, M. D., Gregory, J. M., Bagge, M., Calvert, D., Hagedoorn, J. M., Howard, T., et al. (2020). Exploring the drivers of global and local sea-level change over the 21st century and beyond. *Earth's Future*, *8*(9), e2019EF001413. https://doi.org/10.1029/2019ef001413

Ponte, R. M. (2006). Low-frequency sea level variability and the inverted barometer effect. *Journal of Atmospheric and Oceanic Technology*, *23*(4), 619–629. https://doi.org/10.1175/jtech1864.1

Rencher, A. C. (2005). *A review of "methods of multivariate analysis, Second Edition"* (pp. 1083–1085). Taylor & Francis. https://doi.org/10.1080/07408170500232784

Sajidh, C. K., & Chatterjee, A. (2023). Indian Ocean dynamic sea level, its variability and projections in CMIP6 models. *Climate Dynamics*, *61*(5–6), 2229–2252. https://doi.org/10.1007/s00382-023-06676-z

Sallenger, A. H., Doran, K. S., & Howd, P. A. (2012). Hotspot of accelerated sea-level rise on the Atlantic coast of North America. *Nature Climate Change*, *2*(12), 884–888. https://doi.org/10.1038/nclimate1597

Sannino, G., Carillo, A., Iacono, R., Napolitano, E., Palma, M., Pisacane, G., & Struglia, M. (2022). Modelling present and future climate in the Mediterranean Sea: A focus on sea-level change. *Climate Dynamics*, *59*(1–2), 357–391. https://doi.org/10.1007/s00382-021-06132-w

Séférian, R., Nabat, P., Michou, M., Saint-Martin, D., Voldoire, A., Colin, J., et al. (2019). Evaluation of CNRM earth system model, CNRM-ESM2-1: Role of earth system processes in present-day and future climate. *Journal of Advances in Modeling Earth Systems*, *11*(12), 4182–4227. https://doi.org/10.1029/2019MS001791

Slangen, A. B. A., Meyssignac, B., Agosta, C., Champollion, N., Church, J. A., Fettweis, X., et al. (2017). Evaluating model simulations of twentieth-century sea level rise. Part I: Global mean sea level change. *Journal of Climate*, *30*(21), 8539–8563. https://doi.org/10.1175/jcli-d-17-0110.1

Smeed, D. A., Josey, S., Beaulieu, C., Johns, W., Moat, B. I., Frajka-Williams, E., et al. (2018). The North Atlantic Ocean is in a state of reduced overturning. *Geophysical Research Letters*, *45*(3), 1527–1533. https://doi.org/10.1002/2017gl076350

Sreeraj, P., Swapna, P., Krishnan, R., Nidheesh, A. G., & Sandeep, N. (2022). Extreme sea level rise along the Indian Ocean coastline: Observations and 21st century projections. *Environmental Research Letters*, *17*(11), 114016. https://doi.org/10.1088/1748-9326/ac97f5

Sweet, W., Simon, S., Dusek, G., Marcy, D., Brooks, W., Pendleton, M., & Marra, J. (2021). 2021 state of high tide flooding and annual outlook.

Wang, J., Church, J. A., Zhang, X., & Chen, X. (2021). Reconciling global mean and regional sea level change in projections and observations. *Nature Communications*, *12*(1), 990. https://doi.org/10.1038/s41467-021-21265-6

Wdowinski, S., Bray, R., Kirtman, B. P., & Wu, Z. (2016). Increasing flooding hazard in coastal communities due to rising sea level: Case study of Miami Beach, Florida. *Ocean & Coastal Management*, *126*, 1–8. https://doi.org/10.1016/j.ocecoaman.2016.03.002

Wilson, L. J., Fulton, C. J., Hogg, A. M., Joyce, K. E., Radford, B. T., & Fraser, C. I. (2016). Climate-driven changes to ocean circulation and their inferred impacts on marine dispersal patterns. *Global Ecology and Biogeography*, *25*(8), 923–939. https://doi.org/10.1111/geb.12456

Wöppelmann, G., & Marcos, M. (2016). Vertical land motion as a key to understanding sea level change and variability. *Reviews of Geophysics*, *54*(1), 64–92. https://doi.org/10.1002/2015rg000502

Yin, J. (2023). Rapid decadal acceleration of sea level rise along the U.S. East and Gulf coasts during 2010–22 and its impact on hurricane-induced storm surge. *Journal of Climate*, *36*(13), 4511–4529. https://doi.org/10.1175/jcli-d-22-0670.1

Zhou, M., & Wang, S. (2024). The risk of concurrent heatwaves and extreme sea levels along the global coastline is increasing. *Communications Earth & Environment*, *5*(1), 144. https://doi.org/10.1038/s43247-024-01274-1

References From the Supporting Information

Bentsen, M., Oliviè, D. J. L., Seland, Ø., Toniazzo, T., Gjermundsen, A., Graff, L. S., et al. (2019). *NCC NorESM2-MM model output prepared for CMIP6 CMIP abrupt-4xCO2*. Earth System Grid Federation. https://doi.org/10.22033/ESGF/CMIP6.7840

Boucher, O., Denvil, S., Levavasseur, G., Cozic, A., Caubel, A., Foujols, M.-A., et al. (2019). *IPSL IPSL-CM6A-LR model output prepared for CMIP6 ScenarioMIP ssp119*. Earth System Grid Federation. https://doi.org/10.22033/ESGF/CMIP6.5261

Consortium, E. C.-E. (2019). *EC-Earth-Consortium EC-Earth3-Veg model output prepared for CMIP6 CMIP abrupt-4xCO2*. Earth System Grid Federation. https://doi.org/10.22033/ESGF/CMIP6.4524

Consortium, E. C.-E. (2020a). *EC-Earth-Consortium EC-Earth3-Veg-LR model output prepared for CMIP6 CMIP historical*. Earth System Grid Federation. https://doi.org/10.22033/ESGF/CMIP6.4707

Consortium, E. C.-E. (2020b). *EC-Earth-Consortium EC-Earth3 model output prepared for CMIP6 DCPP dcppC-amv-neg*. Earth System Grid Federation. https://doi.org/10.22033/ESGF/CMIP6.4569

Consortium, E. C.-E. (2021). *EC-Earth-Consortium EC-Earth-3-CC model output prepared for CMIP6 CMIP piControl*. Earth System Grid Federation. https://doi.org/10.22033/ESGF/CMIP6.4844

Fogli, P. G., Iovino, D., & Lovato, T. (2020a). *CMCC CMCC-CM2-HR4 model output prepared for CMIP6 OMIP OMIP2*. Earth System Grid Federation. https://doi.org/10.22033/ESGF/CMIP6.13235

Fogli, P. G., Iovino, D., & Lovato, T. (2020b). *CMCC CMCC-CM2-SR5 model output prepared for CMIP6 OMIP OMIP2*. Earth System Grid Federation. https://doi.org/10.22033/ESGF/CMIP6.13236

Lovato, T., Peano, D., & Butenschön, M. (2021). *CMCC CMCC-ESM2 model output prepared for CMIP6 C4MIP 1pctCO2-bgc*. Earth System Grid Federation. https://doi.org/10.22033/ESGF/CMIP6.13170

Neubauer, D., Ferrachat, S., Siegenthaler-Le Drian, C., Stoll, J., Folini, D. S., Tegen, I., et al. (2019). *HAMMOZ-Consortium MPI-ESM1.2-HAM model output prepared for CMIP6 AerChemMIP hist-piAer*. Earth System Grid Federation. https://doi.org/10.22033/ESGF/CMIP6.5007

Savita, A., Marsland, S., Dix, M., Bi, D., Dobrohotoff, P., Fiedler, R., et al. (2019). *CSIRO-ARCCSS ACCESS-CM2 model output prepared for CMIP6 FAFMIP faf-heat*. Earth System Grid Federation. https://doi.org/10.22033/ESGF/CMIP6.4262

Schupfner, M., Wieners, K.-H., Wachsmann, F., Steger, C., Bittner, M., Jungclaus, J., et al. (2019). *DKRZ MPI-ESM1.2-HR model output prepared for CMIP6 ScenarioMIP SSP126*. Earth System Grid Federation. https://doi.org/10.22033/ESGF/CMIP6.4397

Shiogama, H., Abe, M., & Tatebe, H. (2019). *MIROC MIROC6 model output prepared for CMIP6 ScenarioMIP ssp119*. Earth System Grid Federation. https://doi.org/10.22033/ESGF/CMIP6.5741

Studies, N. G. I. F. S. (2019a). *NASA-GISS GISS-E2.1G model output prepared for CMIP6 CFMIP abrupt-0p5xCO2*. Earth System Grid Federation. https://doi.org/10.22033/ESGF/CMIP6.6972

Studies, N. G. I. F. S. (2019b). *NASA-GISS GISS-E2.1H model output prepared for CMIP6 CMIP 1pctCO2*. Earth System Grid Federation. https://doi.org/10.22033/ESGF/CMIP6.6951

Studies, N. G. I. F. S. (2019c). *NASA-GISS GISS-E2.2H model output prepared for CMIP6 CMIP piControl*. Earth System Grid Federation. https://doi.org/10.22033/ESGF/CMIP6.15874

Swart, N. C., Cole, J. N. S., Kharin, V. V., Lazare, M., Scinocca, J. F., Gillett, N. P., et al. (2019). *CCCma CanESM5 model output prepared for CMIP6 CMIP 1pctCO2*. Earth System Grid Federation. https://doi.org/10.22033/ESGF/CMIP6.3151

Swart, N. C., Cole, J. N. S., Kharin, V. V., Lazare, M., Scinocca, J. F., Gillett, N. P., et al. (2019). *CCCma CanESM5.1 model output prepared for CMIP6 CMIP piControl*. Earth System Grid Federation. https://doi.org/10.22033/ESGF/CMIP6.17424

Tjiputra, J., Schwinger, J., Seland, Ø., Bentsen, M., Oliviè, D. J. L., Toniazzo, T., et al. (2019). *NCC NorESM2-LM model output prepared for CMIP6 CDRMIP 1pctCO2-cdr*. Earth System Grid Federation. https://doi.org/10.22033/ESGF/CMIP6.13725

Volodin, E., Mortikov, E., Gritsun, A., Lykossov, V., Galin, V., Diansky, N., et al. (2019). *INM INM-CM4-8 model output prepared for CMIP6 CMIP piControl*. Earth System Grid Federation. https://doi.org/10.22033/ESGF/CMIP6.5080

Wieners, K.-H., Giorgetta, M., Jungclaus, J., Reick, C., Esch, M., Bittner, M., et al. (2019). *MPI-M MPI-ESM1.2-LR model output prepared for CMIP6 CMIP piControl*. Earth System Grid Federation. https://doi.org/10.22033/ESGF/CMIP6.6675

Wu, T., Chu, M., Dong, M., Fang, Y., Jie, W., Li, J., et al. (2018). *BCC BCC-CSM2MR model output prepared for CMIP6 CMIP esm-hist*. Earth System Grid Federation. https://doi.org/10.22033/ESGF/CMIP6.2901

Yukimoto, S., Koshiro, T., Kawai, H., Oshima, N., Yoshida, K., Urakawa, S., et al. (2019). *MRI MRI-ESM2.0 model output prepared for CMIP6 CMIP piControl*. Earth System Grid Federation. https://doi.org/10.22033/ESGF/CMIP6.6900

Ziehn, T., Chamberlain, M., Lenton, A., Law, R., Bodman, R., Dix, M., et al. (2019). *CSIRO ACCESS-ESM1.5 model output prepared for CMIP6 C4MIP esm-1pct-brch-2000PgC*. Earth System Grid Federation. https://doi.org/10.22033/ESGF/CMIP6.10483